JGR Planets

RESEARCH ARTICLE
10.1029/2024JE008538

Hydrogen Generation From Ferrous Saponite in Reaction With H_2S-Containing Fluid: Relevance to Early Martian Habitability

Natsumi Noda[1,2], Yasuhito Sekine[1,3,4], Yoshio Takahashi[2], Keisuke Fukushi[3], Hiroshi Sakuma[5], Takahiro Kawai[2], Mayuko Nakagawa[1,6], Norio Kitadai[7], Kristin Johnson-Finn[1,8], and Shawn Erin McGlynn[1,9,10]

[1]Earth-Life Science Institute (ELSI), Institute of Science Tokyo, Tokyo, Japan, [2]Department of Earth and Planetary Science, The University of Tokyo, Tokyo, Japan, [3]Institute of Nature and Environmental Technology, Kanazawa University Kakuma, Kanazawa, Japan, [4]Planetary Plasma and Atmospheric Research Center, Tohoku University Aoba, Sendai, Japan, [5]National Institute for Materials Science, Ibaraki, Japan, [6]Department of Earth and Planetary Science, Institute of Science Tokyo, Tokyo, Japan, [7]Institute for Extra-cutting-edge Science and Technology Avant-garde Research (X-star), Japan Agency for Marine-Earth Science and Technology (JAMSTEC), Yokosuka, Japan, [8]Rensselaer Astrobiology Research and Education (RARE) Center, Rensselaer Polytechnic Institute, Troy, NY, USA, [9]Center for Sustainable Resource Science, RIKEN, Wako, Japan, [10]Blue Marble Space Institute of Science Seattle, Washington, DC, USA

Key Points:

- Chemical reactions between ferrous saponite and volatile-containing hydrothermal fluids are investigated
- In our experiments, molecular hydrogen was generated by the reaction of ferrous saponite and hydrogen sulfide, forming iron sulfide
- Interactions of crustal ferrous saponite with hydrothermal fluids may have provided H_2 on early Mars and other wet rocky planets

Correspondence to:
N. Noda,
natsumi@elsi.jp

Citation:
Noda, N., Sekine, Y., Takahashi, Y., Fukushi, K., Sakuma, H., Kawai, T., et al. (2025). Hydrogen generation from ferrous saponite in reaction with H_2S-containing fluid: Relevance to early Martian habitability. *Journal of Geophysical Research: Planets*, *130*, e2024JE008538. https://doi.org/10.1029/2024JE008538

Received 25 JUN 2024
Accepted 28 NOV 2024

Author Contributions:
Conceptualization: Natsumi Noda, Yasuhito Sekine
Data curation: Natsumi Noda
Formal analysis: Natsumi Noda, Takahiro Kawai, Mayuko Nakagawa
Funding acquisition: Natsumi Noda, Yasuhito Sekine
Investigation: Natsumi Noda
Methodology: Natsumi Noda, Yoshio Takahashi, Keisuke Fukushi, Hiroshi Sakuma, Takahiro Kawai, Mayuko Nakagawa, Norio Kitadai, Kristin Johnson-Finn
Project administration: Yasuhito Sekine
Resources: Yoshio Takahashi, Norio Kitadai
Software: Yoshio Takahashi
Supervision: Yasuhito Sekine
Visualization: Natsumi Noda
Writing – original draft: Natsumi Noda, Yasuhito Sekine

Abstract Molecular hydrogen is an important gas species for understanding the early Martian climate and redox chemistry. Through ancient aqueous alterations of crustal rocks, ferrous (Fe(II)) saponite formed abundantly on Mars. Subsequent intrusions of hydrothermal fluids may have resulted in a chemical reaction between the dissolved volatiles and the nearby rocks. Here we propose a new H_2 generating reaction between ferrous saponite and H_2S-containing fluids, which is possible on early Mars. A series of hydrothermal experiments at a relatively low temperature of 90°C were performed under anoxic conditions using synthesized ferrous saponite to compare the resulting H_2 concentration among various gas and fluid compositions. Based on the relationship with the existence of H_2S, reaction time, fluid pH, dissolved iron concentration, and amount of minerals, we found that high levels of H_2 (~0.1 mmol/g ferrous saponite) were generated in the presence of H_2S most rapidly in moderate pH conditions. Our microscopic chemical analysis of mineral phases suggested that ferrous saponite served as both the iron source of pyrite precipitation and the electron source to form H_2. Our results suggest that intrusions of H_2S-containing fluids into the saponite-containing crust of Mars would generate H_2, which could potentially provide locally concentrated chemical energy for chemoautotrophic life.

Plain Language Summary How did early Mars maintain liquid water on its surface? How much chemical energy was available in the aqueous environments? Molecular hydrogen (H_2) is a key molecule that can address these questions concerning Martian habitability because it would have been an effective greenhouse gas and could also provide chemical energy for primitive microbial life. While previous studies have suggested that bolide impacts, volcanoes, and iron oxidation in surface water could have generated H_2 on Mars, we propose a new mechanism that generates H_2 through the interactions of clay minerals with hydrothermal fluids. Clay minerals are widely distributed in the Martian crust we observe today. Our experiments suggest that if hydrothermal fluids containing volcanic hydrogen sulfide (H_2S) had intruded into the clay-bearing crust, H_2 would have been generated.

1. Introduction

Mars has been a unique extraterrestrial target for exploring aqueous chemistry and planetary habitability since geological evidence for the prolonged presence of liquid water on its surface dating back to ~4 billion years ago (Ga) was reported (e.g., Howard et al., 2005; Fassett & Head, 2008). Despite geological evidence, climate models have indicated that achieving a continuously warm climate on early Mars is challenging without a significant supply of greenhouse gas into the atmosphere considering the faint young Sun and the condensation of dense CO_2 atmosphere (Forget et al., 2013; Kasting, 1991; Wordsworth et al., 2013). In addition to the greenhouse effects of atmospheric CH_4, NH_3, and SO_2 (Haberle, 1998; Johnson et al., 2008), recent studies have proposed that the presence of H_2 at high levels of more than several % could effectively warm the surface via collision induced

Writing – review & editing: Yasuhito Sekine, Yoshio Takahashi, Keisuke Fukushi, Hiroshi Sakuma, Mayuko Nakagawa, Norio Kitadai, Kristin Johnson-Finn, Shawn Erin McGlynn

absorptions (CIAs) with CO_2 atmosphere (e.g., Ramirez et al., 2014; Batalha et al., 2015; Turbet et al., 2017, 2020; Wordsworth et al., 2017, 2021). A continuous H_2 supply into the Martian atmosphere is required to maintain a commensurate level against hydrogen escape into space (Batalha et al., 2015; Ramirez et al., 2014). One promising H_2 source on early Mars is volcanic outgassing from the reduced mantle (Gaillard et al., 2013; Righter et al., 2008). Asteroidal impacts (Haberle et al., 2019), serpentinization of mafic igneous rocks (Chassefière et al., 2013, 2016), magnetite authigenesis within lakes (Tosca et al., 2018), and radiolysis of H_2O ice (Tarnas et al., 2018) have also been discussed as sources of H_2. Investigating additional H_2 formation mechanisms, which could have existed in parallel, is important for reconstructing the climate on early Mars.

In addition to the effect on climate, H_2 could have also played an important role in habitability on Mars by providing chemical energy for chemoautotrophic life. Redox reactions between H_2 and CO_2 provide metabolic energy for methanogens and acetogens (e.g., McCollom & Shock, 1997; Fuchs, 2011). For example, the growth of methanogens in laboratory experiments is supported by H_2 slightly lower than 100 ppm with a reaction energy of ~ -20 kJ/mol (Cord-Ruwisch et al., 1988; Zinder, 1993). Given the observations that metabolisms of terrestrial life can be supported by -10 kJ/mol, the potential biological threshold is as low as $\sim$10 ppm H_2, and can be increased depending on other environmental factors such as pH and CO_2 levels (Hoehler et al., 2001; Zinder, 1993). In addition to CO_2, a variety of oxidants, such as oxyhalogens (Hecht et al., 2009; Quinn et al., 2013), O_2 (Koyama et al., 2021; Lanza et al., 2016; Noda et al., 2019), O_3 (Chaffin et al., 2017), SO_3, and NO_2 (Zolotov & Mironenko, 2007), might have been generated on early Mars via photochemical reactions. Reactions of H_2 with these oxidants could have provided chemical energy for chemoautotrophic life in a similar way as occurs in some terrestrial hot spring environments, where H_2 oxidation is coupled with species including O_2, NO_3^-, Fe^{III}, As^V, S°, SO_4^{2-}, and CO_2 (Inskeep et al., 2005).

Here we propose a new process of H_2 generation on early Mars, focusing on ferrous (Fe(II)) saponite, a smectite clay mineral, in the crustal rocks as a reductant for the formation of H_2. The global distribution and chemical composition of Mg/Fe smectite within the Martian crust have been determined using orbital observations (Carter et al., 2013; Ehlmann et al., 2008, 2009, 2011; Fukushi et al., 2019, 2022; Michalski et al., 2015; Mustard et al., 2008; Noda et al., 2022; Poulet et al., 2005; Rampe et al., 2020). A comparison of laboratory analog analysis and remote sensing data indicated that there would be two types of predominant Mg/Fe smectite on Mars: Fe(II)-bearing trioctahedral smectite (ferrous saponite) and Fe(III)-bearing trioctahedral smectite (ferrian saponite), which can be produced by oxidation of ferrous saponite (Chemtob et al., 2017; Michalski et al., 2015). The Curiosity rover has also detected ferrian saponite in the sedimentary rocks of Gale Crater using an X-ray diffraction (XRD) spectrometer, CheMin (Bristow et al., 2015; Treiman et al., 2014; Vaniman et al., 2014). These Mg/Fe smectites are interpreted to have mostly formed ferrous saponite through early aqueous alterations of the Fe-rich mafic composition of the Martian crust and then partially experienced oxidation to form ferrian saponite in the later geological history of Mars (e.g., Catalano, 2013; Ehlmann et al., 2011; Michalski et al., 2013). The global formation of ferrous saponite under a steam atmosphere during magma ocean cooling is also suggested by experiments at H_2O-CO_2 super critical condition (i.e., temperature and pressure condition of 425°C and 300 bar; Cannon et al., 2017).

Although aqueous reactions involving various Fe(II)-bearing minerals expected on early Mars, such as green rust, have been discussed (Tosca et al., 2018), it is unknown whether ferrous saponite can act as a reductant for proton reduction to form molecular hydrogen. Despite the relevance and occurrence of ferrous saponite on Earth (Badaut et al., 1985; Kohyama et al., 1973), investigations of its ability to act as a reductant have been limited because of its sensitivity to oxidation by O_2 in the atmosphere (Noda et al., 2021; O'Loughlin et al., 2020). Several previous studies have examined the formation and alteration processes of ferrous saponite on early Mars using synthesized ferrous saponite (e.g., Chemtob et al., 2017; Noda et al., 2021; Rivera Banuchi et al., 2022; Sakuma et al., 2022); however, H_2 production from ferrous saponite has not been discussed. The global occurrence of deep hydrothermal circulation reactive with the surrounding crust of early Mars has been proposed according to geomorphological (e.g., fluvial features at deep craters) and mineralogical (e.g., clay units exposed at heavily eroded terrain) records and supported by hydrological calculations (Andrews-Hanna et al., 2007; Ehlmann et al., 2011; Kite & Melwani Daswani, 2019; Michalski et al., 2013; Ojha et al., 2020; Salese et al., 2019). Thus, the crustal ferrous saponite could have interacted with an intruded anoxic hydrothermal fluid that dissolves degassing components such as carbon and sulfur volatiles.

In this study, we experimentally investigated the interactions between ferrous saponite and volatile (i.e., CO_2 and H_2S) containing fluid. Hydrothermal experiments were conducted under anoxic conditions with various fluid compositions and pH values to constrain mechanisms of H_2 generating reactions.

2. Methods

2.1. Synthetic Ferrous Saponite

The ferrous saponite samples used in this study were synthesized using a sol-gel method within decomposition vessels (HU-100, San-Ai Kagaku Co., Ltd., Aichi, Japan) in an acrylic glovebox connected to a deoxygenation system (SiOC-2000 GB; STLab Co., Ibaraki, Japan), as described elsewhere (Noda et al., 2021). Anoxic conditions with an oxygen level (P_{O_2}) of <0.01 ppb and humidity ∼50% were maintained throughout all sample preparations and collection procedures. Ultrapure water (Milli-Q; Millipore) was bubbled with Ar gas (>99.999 vol.%, Suzuki Shokan, Kanagawa, Japan) at 2.8 L min^{-1} for 3 hr in the glovebox prior to use so as to reduce its dissolved oxygen (DO) below 0.01 ppm (Noda et al., 2021). Throughout the synthesis procedure, oxidation of Fe^{2+} was effectively prohibited: the characterized saponite was only ∼4% $Fe^{3+}/\Sigma Fe$ (Noda et al., 2021).

The ideal half-cell formula described as $Na_{0.5}(Mg_{1.5}Fe^{2+}_{1.5})(Si_{3.5}Al_{0.5})O_{10}(OH)_2$ corresponds well to orbiters' and rovers' analyses of Martian clay minerals (Michalski et al., 2015). We aimed at achieving this composition by mixing the reagents (Na_4SiO_4, $FeSO_4 \cdot 7H_2O$, $MgCl_2 \cdot 6H_2O$, and $AlCl_3 \cdot 6H_2O$; Noda et al., 2021) in a proper molar ratio. The intended Fe/Mg M ratio (∼1.0) was confirmed using scanning electron microscopy and energy-dispersive X-ray spectrometry (SEM-EDS; S-3400N; Hitachi High-Tech Corp., Japan). The synthesized ferrous saponite was dried and powdered in the glovebox using an agate mortar so that the typical grain size ranges 1–100 μm, followed by sealing within high-barrier nylon/polyethylene storage bags with oxygen absorbers (Oxygen-Free, Dried Storage System, A-500-50S; I.S.O. Inc., Kanagawa, Japan).

2.2. Anoxic Gas–Fluid–Mineral-Phase Reaction

Crimp-top glass vials (effective volume of approximately 70 mL; Vial Bottle No. 7; Maruemu Corp., Osaka, Japan) sealed with Al-capped Teflon-laminated butyl stoppers (5-112-07; AS ONE Corp., Osaka, Japan) were used as reaction vessels to encapsulate various mineral, fluid, and gas phases as initial conditions (Table 1). Both the glass vials and stoppers were pre-cleaned by soaking in ∼4 M HNO_3 at room temperature (∼25°C) for 70 hr and then in ultrapure water for 60 hr. The glass vials were then heated in an electric furnace (FO410; Yamato Science, Tokyo, Japan) at 450°C for 12 hr.

Solutions of sodium bicarbonate were prepared in the glove box from the deoxidized ultrapure water (DO < 0.01 ppm) for the fluid phases. Sodium bicarbonate ($NaHCO_3$, Guaranteed Reagent; Wako Pure Chemical Industries) was used because dissolved bicarbonates and CO_2 gas can act as pH buffers (i.e., bicarbonate-carbonate buffer system). After the crimp-sealing of the vials with typically 100 ± 3 mg of mineral powders and ∼10 mL of fluids, the headspace was purged with either pure Ar (>99.999 vol.%; Suzuki Shokan) or CO_2 gas (>99.999 vol.%; Suzuki Shokan) at 100 mL min^{-1} for 5 min. The headspace gas phase accounted for ∼60 ml in a ∼70 ml vial.

In some of the experiments, H_2S was introduced into glass vials containing minerals and fluids (see Section 2.3). H_2S was prepared based on the methodology shown in the previous work (Kitadai et al., 2021) with the following reaction:

$$Na_2S + 2HCl \rightarrow 2NaCl + H_2S. \quad (1)$$

To make H_2S, precleaned vials containing 1.0 g of hydrated sodium sulfide ($NaS_2 \cdot 9H_2O$; Kishida Chemical Co. Ltd., Osaka, Japan) were evacuated to <50 Pa and sealed in advance using a drying chamber (FDU-1200, BSC-2L; Tokyo Rikaki Co., Ltd., Tokyo, Japan). Then, ∼1.2 mL of 6 M HCl (Wako Pure Chemical Industries) was added so that the vial volume of ∼70 mL would be filled with generated H_2S gas at the ambient temperature and pressure. Using a gas-tight syringe (SGE Analytical 10MDR-VLLMA-GT; Trajan Scientific Japan, Kanagawa, Japan), 10 mL of the generated H_2S gas was injected into each experimental vial after removing the same volume of purged CO_2 or Ar gas.

All the crimped vials containing mineral, fluid, purged gas, and H_2S were moved from the glovebox into a forced-convection drying oven (ETTAS OFW-450V; AS ONE) kept at a constant temperature of 90 ± 1°C. Geothermal

Table 1
Initial Conditions for Respective Groups of Experiments

	Number of runs	Duration (h)	Mineral Mass (mg)[a]	Fluid Mass (g)[b]	Fluid $NaHCO_3$ (mM)[c]	Fluid HCl (mM)[c]	Headspace gas Purged gas	Headspace gas H_2S injection[d]	Fluid pH[e]
Control 1	3	863–975	–	10.2	–	–	Ar	+	5.7–6.2
Control 2	3	420–421	–	10.1	1.00×10^2	–	CO_2	+	7.0–7.2
	1	94							
Mineral species									
Ferrous saponite	3	429–438	100	10.4	1.00×10^2	–	CO_2	+	7.2–7.3
Magnetite	3	422–438	102	10.4	1.00×10^2	–	CO_2	+	7.0–7.7
	1	1,533							
Troilite	3	420–422	101	10.0	0.99×10^2	–	CO_2	+	7.1–7.6
Iron-nickel alloy	3	303–305	100	10.2	0.99×10^2	–	CO_2	+	7.1–7.2
Ferrous saponite	3	420–443	96	10.0	1.00×10^2	–	CO_2	–	7.0–7.2
Magnetite	3	438–443	98	10.0	1.00×10^2	–	CO_2	–	7.0–7.5
	1	1,500							
Troilite	3	420–422	102	10.0	0.98×10^2	–	CO_2	–	7.0–7.1
Iron-nickel alloy	3	303–305	101	10.1	0.98×10^2	–	CO_2	–	7.1–7.2
Group									
I	5	34–1,791	100	10.0	–	–	Ar	+	8.4–9.4
i	7	29–1,774	27	10.0	–	–	Ar	+	6.8–7.5
II	5	34–1,791	101	10.1	1.00×10^2	–	CO_2	+	7.0–7.2
ii	7	29–1,780	27	10.1	1.00×10^2	–	CO_2	+	7.0–7.2
III	5	35–1,740	101	10.0	–	–	CO_2	+	6.3–6.8
iii	7	29–1,738	27	10.1	–	–	CO_2	+	5.7–6.1
IV	5	29–1,774	100	10.0	0.98×10^2	0.98×10^2	CO_2	+	6.2–6.8
iv	5	29–1,749	26	10.1	0.99×10^2	0.50×10^2	CO_2	+	6.7–6.8
V	6	29–1,780	100	10.0	–	–	CO_2	–	6.3–6.6
v	4	29–1,355	27	10.1	1.00×10^2	–	CO_2	–	7.0–7.3

Note. The experiments for comparison among different mineral species (above) and for comparison of time evolution among various initial conditions (below). As for the latter, the resulted fluid pH measured after the experiment are also included. [a]The weighing accuracy was ±3 mg. [b]The accuracy was within ±0.3 g. [c]The accuracy was estimated to be ±2% of the value. The symbol "–" indicates that the species was not included. [d]The symbol "+" indicates that 10 mL in ∼60 mL of purged gas was exchanged to H_2S gas, while the symbol "–" indicates that the whole headspace remained filled with purged gas. [e]The lowest and highest values among the independent runs in the group with different reaction times are shown. The accuracy of each pH measurement was ±0.1.

estimates on the Noachian Martian crust have suggested that hydrothermal alteration at 90°C is presumable at a few to ∼5 km depth from the near-freezing surface (Michalski et al., 2013; Ojha et al., 2020). By referencing previous hydrothermal experiments with iron-bearing minerals using similar experimental setups (Barge et al., 2019; Heinen & Lauwers, 1996), we considered 90°C to represent the reaction procedure in the experimental timescale of the present study. For comparison, two vials with ferrous saponite and H_2S injection were placed at the ambient temperature (∼23°C). To minimize gas leaks and air contaminations during the incubation, the vials were placed in the oven with the top side facing downward to ensure that the fluid covered the rubber stoppers.

2.3. Experimental Conditions

First, we conducted comparative hydrothermal experiments on various mineral types. In these experiments, we found H_2 production specific for the co-existence of ferrous saponite and gaseous H_2S (see Section 3.1 below).

Then, we explored the time evolution of the H_2 production via interactions with ferrous saponite with H_2S-containing fluids with different gas and fluid compositions to investigate the reaction mechanisms.

In the comparative hydrothermal experiments, 4 types of Fe-bearing minerals, that is, synthesized ferrous saponite, magnetite (Fe_3O_4, 95.0+%; Wako Pure Chemical Industries, Osaka, Japan), troilite (FeS, Practical Grade; Wako Pure Chemical Industries) and iron-nickel alloy (Fe:Ni = 90:10 wt.%, 99.9% purity; Kojundo Chemical Laboratory, Saitama, Japan), were compared with and without H_2S (Table 1). Two types of control experiments without minerals were also conducted: one with Ar gas, pure water, and H_2S injection, and the other with the bicarbonate-carbonate buffer system and H_2S injection (Table 1). The headspace gas composition was analyzed typically after ~400 hr of incubation. In addition to three time runs each, one with different reaction time were analyzed in some conditions. The Fe-bearing materials other than ferrous saponite (magnetite, troilite, and Fe-Ni alloy) correspond to (hydr)oxide, sulfide, and metal possibly available on Mars, whose aqueous reactions have been discussed in simulating paleoenvironments of Mars and Earth (e.g., Haberle et al., 2019; Heinen & Lauwers, 1996; Tosca et al., 2018). The Curiosity rover detected magnetite and a low level of pyrite within the lake deposition (Vaniman et al., 2014). The reaction between pyrite and H_2S has been demonstrated and proposed as a plausible H_2 source in the reducing paleoenvironment on Earth (Heinen & Lauwers, 1996). Iron contained in meteorites could have been oxidized by water, providing significant H_2 into the early Martian atmosphere temporarily after impacts (Haberle et al., 2019; Wordsworth et al., 2021).

In terms of the time evolution of H_2 production from ferrous saponite, 10 groups of experiments (groups I–V and i–v) with different gas and fluid compositions were compared (Table 1). Groups i–v contained lower amounts of ferrous saponite (27 mg) than groups I–V (100 mg) (Table 1). In group I and i experiments, Ar gas was introduced instead of CO_2. In the group II–IV and ii–iv experiments, CO_2, $NaHCO_3$ and/or HCl were introduced in different amounts so that different pH and ionic strengths were tested (Table 1). Group V and v experiments contained no H_2S to compare against samples containing sulfide (Table 1). Each group comprised four to seven individual runs with reaction times ranging from 30 to 1,800 hr. Analysis of each run (i.e., gas measurement and collection of fluid and mineral samples) was done only once after the given reaction time with a few exceptions in respective groups for gas measurement. Blank experiments without minerals, CO_2, and H_2S were performed in duplicate with long reaction times (~900 hr) to check the background detection levels of gas species from the reaction of water with the glass vials.

2.4. Gas and Liquid Analyses

The concentrations of H_2 in the headspace gas of the glass vials were determined using Gas Chromatography with Barrier-discharge Ionization Detector (GC-BID; GC-2010 Plus, BID-2010 Plus; Shimadzu, Kyoto, Japan) and Micropacked-ST column (2.0 m × 1.0 mm I.D.; Shinwa chemical Industries), with an initial temperature of 35°C (held 9 min) ramped to 100°C at 16°C min^{-1} (held 4 min), then to 150°C at 22°C min^{-1} (held 10 min). Headspace gas was collected and injected manually using a gas-tight syringe (A-2; Valco Instruments, TX, USA). The concentration of H_2 was quantified based on the chromatogram peak area and the injection volume ((40–100) ± 0.5 μL). The error and the lower limit of quantitation were derived from uncertainties in peak detection, calibration line, and injection volume.

After incubation and gas analysis, the fluid and mineral samples for subsequent analysis were collected in the glovebox. The mixture of fluid and mineral phases collected with disposable PP syringes (SS-10LZ; Terumo Corp.; Tokyo, Japan) was separated using a membrane filter (0.2 μm PTFE Membrane JGWP02500 or 0.025 μm MCE Membrane VSWP02500; Merck Millipore Ltd., Darmstadt, Germany) placed in a filter holder (Swinnex Filter Holder Φ25 mm SX0002500; Merck Millipore Ltd., Darmstadt, Germany). Mineral samples gathered on the filter were vacuum-dried, placed in microtubes, and sealed in the oxygen-free storage bags. The pH of the filtered fluid was measured at room temperature using a pH meter (LAQUA twin pH-22B; Horiba Co., Ltd.) calibrated prior to use. In the experiments, minerals, including ferrous saponite, partly dissolved, releasing Na, Al, Si, Mg, and Fe into fluids. The concentrations of dissolved Fe and Mg in the fluid were measured using inductively coupled plasma–atomic emission spectrometry (ICP–AES; SPS5510; SII NanoTech, Tokyo, Japan). The collected fluid samples were diluted ~8-fold in precleaned polypropylene vials with 0.1 M HNO_3 prepared by diluting 68 wt.% HNO_3 ultrapure analytical reagent (TAMAPURE-AA-100; Tama Chemicals Co., Ltd.) with ultrapure water. The diluted standard solutions (XSTC-622; SPEX CertiPrep, LLC.) were prepared and analyzed for calibration.

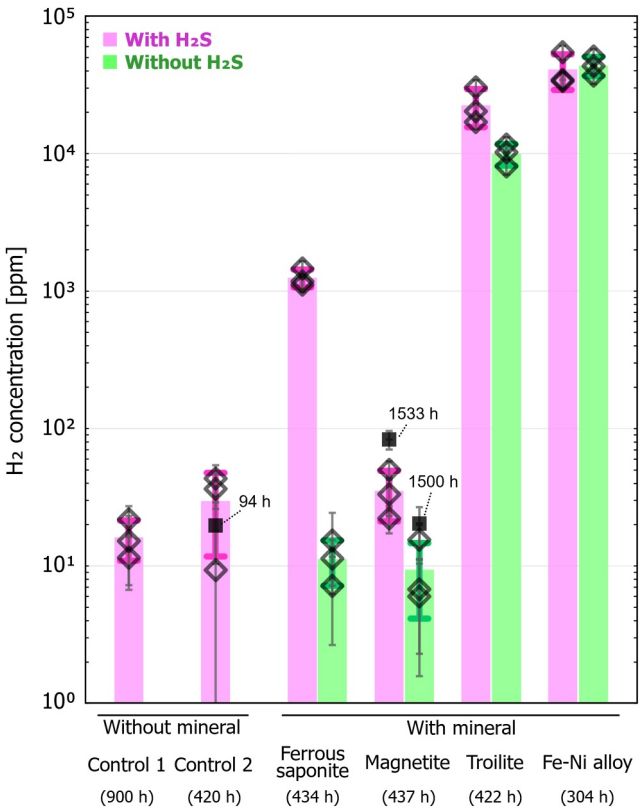

Figure 1. Comparison of H_2 concentrations in the headspace gas among the reactions with various minerals. Control experiments without minerals are also shown. Colored bars and errors represent the averages and standard deviations of three repeated experiments, respectively. Their mean reaction times (hours (h)) and mineral names are provided at the bottom of *x*-axis. The color of the bars corresponds to the presence (pink) or absence (green) of H_2S in the initial headspace gas compositions. Open diamonds indicate the results from three individual experiments under the same reaction conditions with quantitation errors. Solid squares show the results with different reaction times from those shown at the bottom of *x*-axis. The initial conditions of the respective experiments are provided in Table 1.

2.5. Chemical Analysis of Mineral Phases

The collected mineral samples were subjected to synchrotron-based chemical analyses in order to visualize changes in the chemical state. In scanning transmission X-ray microscopy (STXM), X-ray absorption near-edge structural (XANES) mapping with a high spatial resolution of about 50 nm was performed. The preparation and analytical procedures for STXM measurements were based on our previous study (Noda et al., 2021). Fine grains of the dried mineral samples were mounted on a 400 mesh Cu grid with a supporting film (No. 1608; JEOL Ltd., Tokyo, Japan), attached to the sample holder, and stored in a dry oxygen-free storage system in the glovebox without any air exposure until STXM analysis (Noda et al., 2021). The stacked images obtained around the Fe L-edge (700–732 eV) were accumulated and converted to extract the XANES spectra at an optical density using the analytical software aXis2000 (Hitchcock, 2009). The XANES spectra of the bulk powdered samples were obtained using Beamline 19B at the Photon Factory for reference. Both the extracted and bulk XANES spectra were analyzed using Athena software v. 0.9.26 (Ravel & Newville, 2005).

3. Results

3.1. Comparison of H_2 Formation for Different Minerals

Figure 1 compares the measured H_2 concentrations with different iron-bearing minerals and without minerals (controls). Among the tested minerals, ferrous saponite showed the most significant difference in H_2 concentration between the presence and absence of H_2S (Figure 1). The highest levels of H_2 ($\sim 4 \times 10^4$ ppm) were produced in the experiment with Fe–Ni alloy regardless of H_2S injection (Figure 1). This is attributed to the reaction of water with metallic Fe (Haberle et al., 2019),

$$Fe^0 + H_2O \rightarrow FeO + H_{2(g)}. \quad (2)$$

Low levels of H_2 ($<10^2$ ppm) were measured in the experiments using magnetite after 400 and 1,500 hr of the experimental time (Figure 1). The H_2 concentrations with H_2S was ~40 ppm higher than those without H_2S, which can be attributed to H_2 contained in the injected H_2S: small amounts of H_2 (<40 ppm in the reaction vial) was found in the prepared H_2S gas as shown in the control experiments (Figure 1), possibly due to the corrosion of the needle used for the injection of HCl. The reaction between water and magnetite could form H_2 and iron hydroxide (e.g., ~0.1 μmol H_2/g mineral at 100°C: Mayhew et al., 2013); however, the fact that the H_2 concentration is comparable to those of the control experiments supports the idea that the contribution of this H_2 generation (~10 nmol of H_2 for 100 mg of magnetite) is small compared to the total H_2 production.

H_2 concentration in the experiment with troilite was about twofold increased by H_2S injection. This can be attributed to the formation of pyrite (FeS_2), as observed under terrestrial aqueous conditions (Heinen & Lauwers, 1996; Rickard, 1997; Wächtershäuser, 1992; Wan et al., 2017),

$$FeS + H_2S \rightarrow FeS_2 + H_{2(g)}. \quad (3)$$

Here, H_2S acts as an electron acceptor due to the fact that FeS has the highest occupied molecular orbital (HOMO; +0.5 eV) less stable than the lowest unoccupied molecular orbital (LUMO) of H_2S (−1.1 eV) (Rickard & Luther, 1997). Relatively high H_2 concentration ($\sim 1 \times 10^4$ ppm) without H_2S injection indicates that water-troilite interaction also forms H_2.

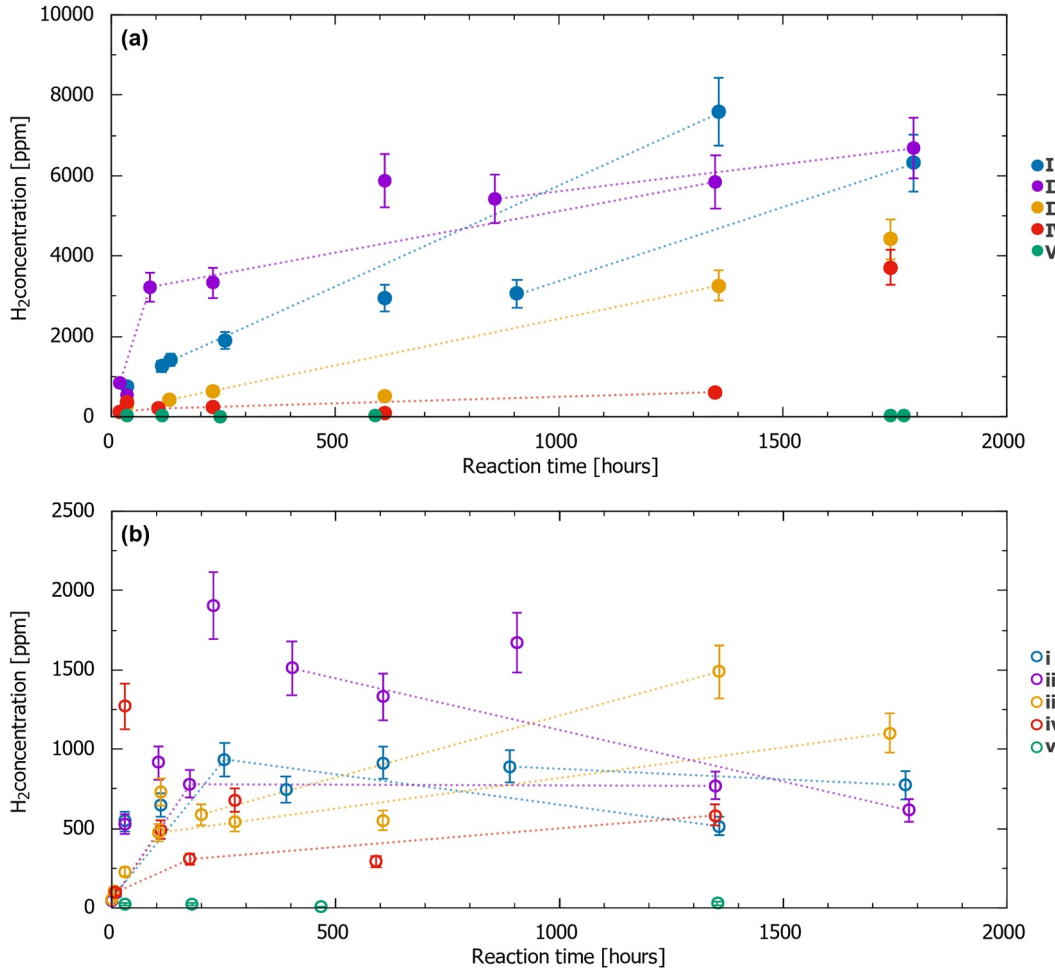

Figure 2. H_2 concentrations in the headspace gas as a function of reaction time for (a) the group I-V experiments (with 100 mg of ferrous saponite) and for (b) the group i-v experiments (27 mg of ferrous saponite). Respective dot lines connect the data from single experiments measured at different reaction times. Except for these, each data point corresponds to a single experiment prepared individually and ended at the indicated reaction time. Error bars show the quantitation uncertainties in peak detection, calibration line, and injection volume. The experimental conditions of the respective groups are provided in Table 1.

Experimental triplicates with synthesized ferrous saponite showed similar H_2 concentrations of $\sim 1 \times 10^3$ ppm with H_2S, which is two orders of magnitude higher than those without H_2S (Figure 1). In contrast to those with troilite, H_2 concentration was limited (<20 ppm) when no H_2S was injected (Figure 1). This significant dependence on the existence of H_2S suggests ferrous saponite is involved directly or catalytically in H_2 generation in the interaction with H_2S. H_2 generating reaction was also confirmed in the experiments performed at ambient temperature (~23°C) instead of 90°C with the same initial composition. The low H_2 concentrations ($\sim 2 \times 10^2$ ppm after ~450 hr reaction; Supplementary Table S1) were consistent with the slow reaction rate at the low temperature than that at 90°C.

3.2. Time Evolution of H_2 Concentration in Reaction With Ferrous Saponite

To further explore the reaction mechanism and the role of ferrous saponite in generating H_2, the different reaction conditions, including fluid pH by varying the gas and fluid compositions and mass of ferrous saponite, were compared (Table 1). Independent 4–7 runs with various reaction times were conducted for each group to measure the resulting concentrations of gaseous H_2 and dissolved Fe and Mg.

H_2 concentration reached $\sim(4-7) \times 10^3$ ppm after the reaction time of 1,750 hr with 100 mg of ferrous saponite and H_2S injection (groups I–IV in Figure 2a). No significant H_2 (<50 ppm) was generated over the reaction time

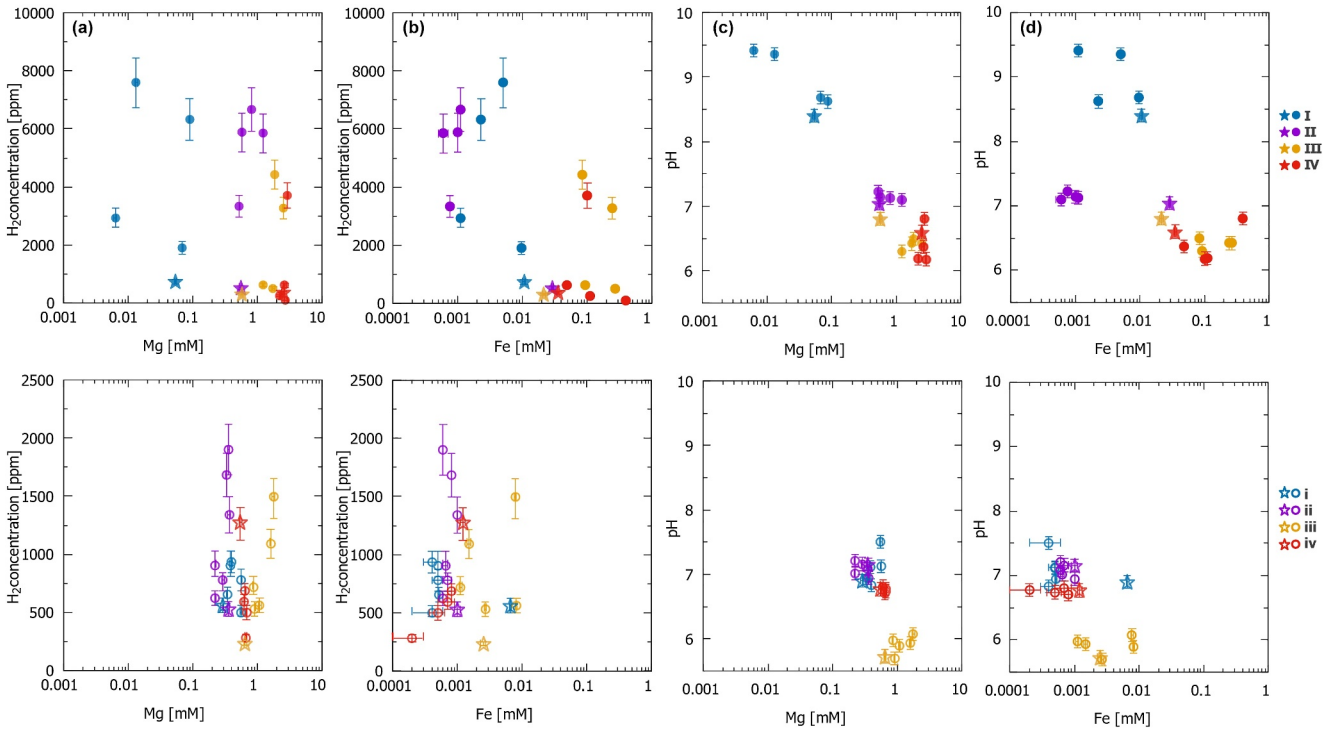

Figure 3. Results of (a, b) H_2 concentrations and (c, d) fluid pH as a function of the concentrations of (a, c) Mg and (b, d) Fe dissolved in the filtered fluid samples. The top panels show data from group I–IV experiments with 100 mg of ferrous saponite, while the bottom panels show group i–iv experiments with 27 mg of ferrous saponite. Each data point represents a single separated experiment that ended at various reaction times (29–1,791 hr). Stars indicate the data from the experiments with the shortest reaction time (29–34 hr) among each experimental group. Error bars show the quantitation uncertainty of each experiment.

of 1,750 hr in the group V experiments without H_2S (Figure 2a), confirming that H_2S is essential in H_2 production from ferrous saponite. The experimental duration required for the H_2 production was different among the group I–IV experiments. Group II showed the most rapid increase in the H_2 concentration in the experiment with a few days (~100–200 hr) and reached a plateau at (6–7) × 10^3 ppm after 600 hr of reaction (Figure 2a). H_2 concentrations also started to increase for a relatively short duration in the group I experiments and reached 8 × 10^3 ppm after 1,350 hr (Figure 2a). Neutral pH values (~7.1) were maintained throughout the reaction time in the group II owing to the bicarbonate-carbonate buffer system; meanwhile, the pH of the group I experiments was alkaline (pH ~8–9) without CO_2 or $NaHCO_3$ (Table 1). Much longer reaction times were required for the H_2 generation in group III and IV experiments with weakly acidic pH (pH ~6.2–6.8) (Table 1). In group III and IV experiments, H_2 concentrations remained low (<7 × 10^2 ppm) in reaction times shorter than 700 hr and then increased to ~ 4 × 10^3 ppm after 1,750 hr reaction (Figure 2a). These results indicate that the fluid pH affected the kinetics of the H_2 production reaction with ferrous saponite.

In the group i-v experiments with lower starting amounts (~27 mg) of ferrous saponite than the group I–V experiments (~100 mg), the H_2 concentration of the group i–v experiments became generally lower than that of the group I–V experiments (Figure 2b). Groups i, ii, and iv had a moderate pH of ~7, despite differences in gas and fluid composition (Table 1). The H_2 concentrations in these groups generally increased to ~(1–2) × 10^3 ppm in the short reaction time within 250 hr and then decreased to ~7 × 10^2 ppm after a longer duration of >1,000 hr (Figure 2b). On the contrary, the group iii experiments at pH ~6 showed a relatively low H_2 concentration of (5–7) × 10^2 ppm in the relatively short experiments of 100–600 hr and increased to >1 × 10^3 ppm after reaction times longer than 1,350 hr (Figure 2b). The observed trend of slower H_2 production under acidic conditions compared to neutral conditions is consistent with the results of larger amounts of ferrous saponite (i.e., the difference between group III and II experiments). Little H_2 was found in group v experiments for all reaction times tested as no H_2S was introduced in the experiments (Figure 2b).

Figure 3 shows the changes in H_2 concentration and fluid pH as a function of Mg and Fe concentrations dissolved in the filtered fluid samples. Low Mg concentrations (<0.1 mM) were measured with an alkaline pH of

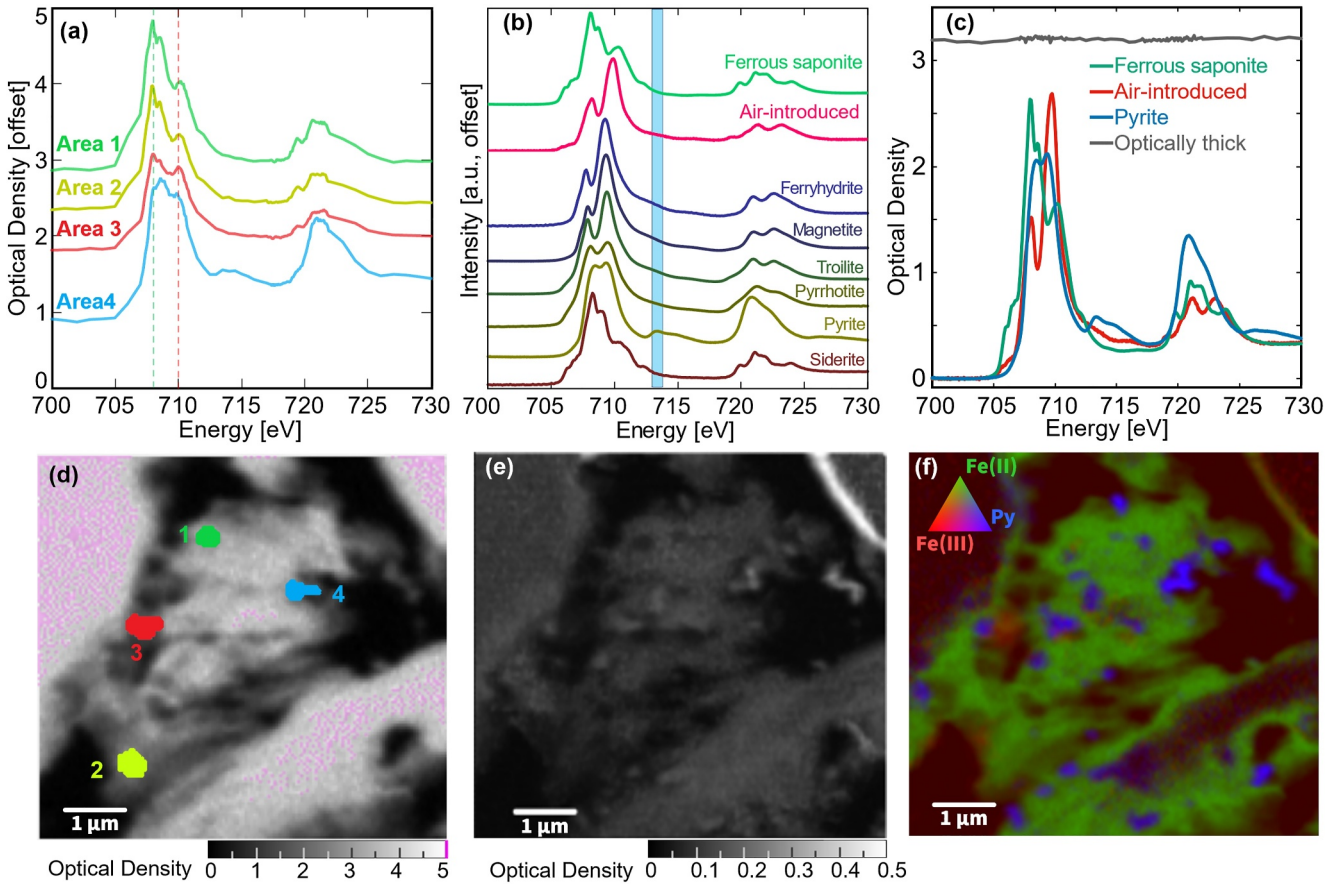

Figure 4. Result of STXM analysis. (a–c) Normalized XANES spectra are calibrated at the absorption edge energy, E_0, of 707.4 eV. (a) Spectra extracted from the area shown in panel (d). Vertical dashed lines correspond to 708 and 710 eV. (b) Bulk XANES spectra of synthesized ferrous saponite stored under anoxic conditions, ferrous saponite oxidized by ambient air, and various Fe-bearing reference minerals. (c) XANES spectra of the endmember components used for SVD mapping of STXM stacked images. (d–f) Results of STXM measurements performed for the mineral sample collected after ~600 hr of reaction for the group ii experiment. (d) Optical density map at a single X-ray energy of 707.4 eV. (e) Residuals of SVD mapping of the stacked image shown in optical density. (f) Results of SVD mapping visualized in RGB color. The relative contributions of the three components in panel (c) are shown, with ferrous saponite in green, air-introduced Fe(III)-bearing saponite in red, and pyrite in blue.

approximately 9 in group I, while high Mg concentrations (~2–3 mM) were observed at pH ~ 6.5 in groups III and IV (Figure 3c, top). Among groups i-iv, group iii with the lowest pH (~5.8) showed the highest Mg concentrations (~1–2 mM) (Figure 3c, bottom). These results show that the Mg concentration is controlled by the fluid pH and is independent of H_2 generation (Figures 3a and 3c). The varied Mg concentration in group I was due to the variation in fluid pH. Since no pH buffer (carbonate-bicarbonate buffer) was used, the fluid pH of group I can be varied depending on small differences in the initial materials among the runs.

In contrast to Mg, Fe concentrations varied with reaction time and were less correlated with pH (Figure 3d) despite the 1:1 molar ratio of Mg and Fe in our synthesized ferrous saponite. Figure 3b indicates that the fluids of groups I–IV shared similar Fe concentrations of $\sim 10^{-2}$ mM at the beginning of the reaction. Then, in the groups I and II experiments, Fe concentrations decreased to $\sim 10^{-3}$ mM in response to increasing H_2 concentrations (Figure 3b, top), suggesting that dissolved Fe could have been consumed by H_2 generating reaction in these experiments. Fe concentrations increased to >0.1 mM in the group III and IV experiments without increases in H_2 concentrations (Figure 3b, top), suggesting that the dissolution of Fe in ferrous saponite did not trigger rapid H_2 generation. Significant H_2 detection with low dissolved Fe concentration ($<\sim 10^{-3}$ mM) at neutral pH condition was also confirmed starting with the smaller amount of saponite (Figure 3b, bottom).

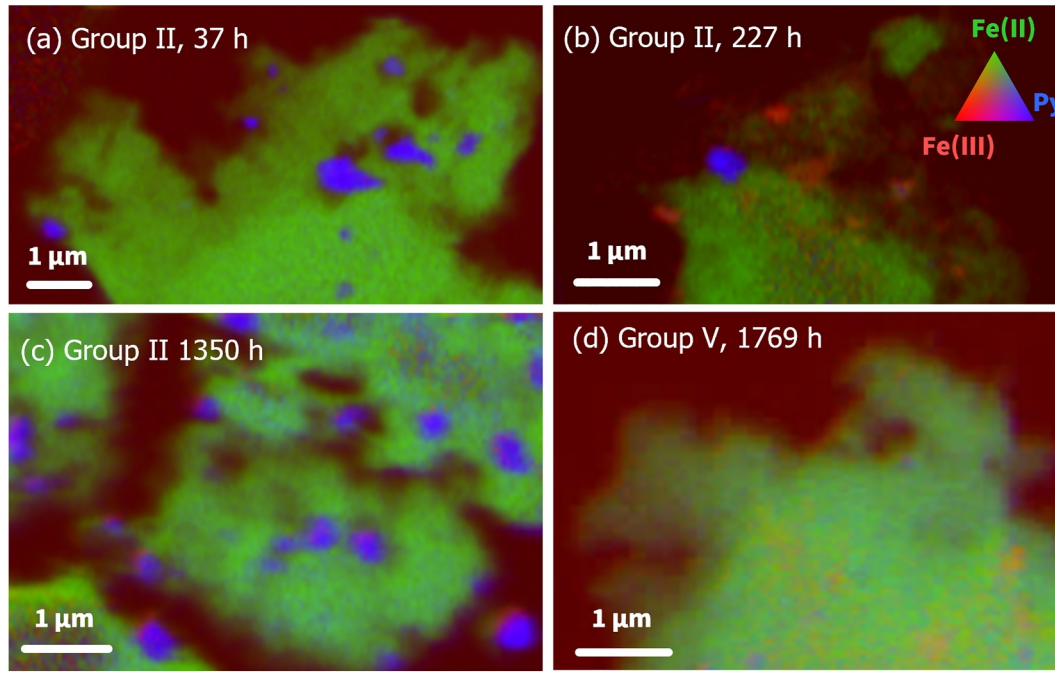

Figure 5. Result of SVD mapping of STXM measurements performed for the mineral sample collected after (a) 37, (b) 227, and (c) 1,350 hr of reaction in the group II experiment, and (d) 1,759 hr of reaction in the group V experiment. The visualization of the stacked image is done in the same condition as Figure 4f. The color represents the relative concentrations of the three endmembers, with ferrous saponite in green, air-introduced Fe(III)-bearing saponite in red, and pyrite in blue.

3.2.1. Characterization of Reactions in the Solid Phase

STXM analysis was performed for the dried mineral samples retrieved from group ii (Figure 4) and II (Figures 5a–5c) experiments, where neutral pH was maintained during rapid H_2 generation. For comparison, the STXM analysis was also performed for the samples of the group V experiment (Figure 5d), where the absence of H_2S resulted in no H_2 detection. The grains with the proper optical thickness were searched and chosen to obtain stacked images.

The strong absorptions in the extracted XANES spectra at around 708 and 710 eV are generally attributed to ferrous and ferric iron, respectively. Most regions exhibited XANES spectra similar to the bulk XANES spectra of synthesized ferrous saponite obtained without any air exposure (area 1 and 2 in Figures 4a and 4d, in comparison with the line labeled "Ferrous saponite" in Figure 4b), while some areas showed relatively high absorption at around 710 eV (area 3 in Figures 4a and 4d). The absorption at 710 eV was significant in the bulk XANES spectra of ferrous saponite exposed to O_2 by introducing ambient air in the reaction vial instead of Ar or CO_2 together with ~10 mL of pure water and kept at 90°C for ~900 hr (the line labeled with "Air-introduced" in Figure 4b). Given the effective aerial oxidation, the absorption at 710 eV should be attributed to Fe(III)-bearing (hydro-)oxide (i.e., ferrihydrite and magnetite; Figure 4b) or Fe(III)-bearing saponite (i.e., ferrian saponite; Chemtob et al., 2015, 2017). Moreover, a broad absorption band at around 714 eV was also found (area 4 in Figures 4a and 4d). This spectral feature only appeared in pyrite (FeS_2) among the various Fe bearing standards we tested, including iron (hydro-)oxide, sulfide, and carbonate (Figure 4b).

The detailed spatial distribution of the chemical states of Fe was visualized using single-value decomposition (SVD) mapping with four endmember components. In addition to the extracted XANES spectra of the optically thick area, the bulk XANES spectra of the synthesized ferrous saponite, aerially oxidized ferrous saponite containing Fe(III), and commercially purchased pyrite were used as endmembers (Figure 4c). The three bulk XANES spectra were normalized to have similar optical densities at the pre- and post-edges to create appropriate color maps (Figure 4c). Using these endmembers, the residuals of the fitting were suppressed to an optical density below 0.5 (Figure 4e), which was minimized using other available references in Figure 4b. The result of SVD mapping shows that sub-micrometer-sized pyrite (blue particles) occurred widely within and beside the ferrous

saponite through the reaction of the group ii experiments (Figure 4f). The presence of Fe(III)-bearing materials (reddish features) surrounding pyrite indicates that ferrous iron oxidation to ferric iron may occur in conjunction with pyrite formation (Figure 4f).

Figures 5a–5c compares the STXM results in the SVD mapping of the group II experiment with different reaction times. After a reaction time of 37 hr, sub-micrometer-sized pyrite particles were first generated in ferrous saponite, while no Fe(III)-bearing areas were found. This indicates that oxidation by air during the experiment and analysis was prevented (Figure 5a). After 227 hr of reaction, Fe(III)-bearing areas started to appear in the sample in addition to pyrite particles (Figure 5b). Fe(III)-bearing areas appeared in the vicinity of pyrite after 1,350 hr of reaction (Figure 5c). Fe(III)-bearing features and pyrite was less significant in the sample from the experiment without H_2S (Figure 5d). The minor Fe(III)-bearing area and pyrite in Figure 5d can be attributed to the uncertainty in SVD fitting. The chemical state of ferrous iron was largely unchanged in the experiments without H_2S (Figure 5d), supporting that the occurrence of Fe(III)-bearing areas in the experiments with H_2S were associated with the H_2 generating reaction.

4. Discussion

4.1. Mechanism for H_2 Generation From H_2S-Containing Fluids With Ferrous Saponite

The results of our experiments, including both comparative hydrothermal experiments (Section 3.1) and time variation experiments (Section 3.2) on the hydrothermal interactions between ferrous saponite and volatile-containing fluids, can be summarized as follows:

1. Ferrous saponite was involved in H_2 generation when it interacted with H_2S containing fluid (Figure 1). Little H_2 detection without H_2S in long incubation experiments strongly suggests that H_2S played an essential role in H_2 production (Figure 2).
2. As for the time variation, H_2 generation occurred most rapidly under circumneutral pH conditions (Figure 2). H_2 production proceeds more slowly under weakly acidic (pH ∼6.5) conditions than under alkaline (pH ∼9) conditions (Figure 2).
3. As for the fluid composition, a decrease in Fe concentration with an increase in H_2 concentration was observed in neutral-alkaline pH, suggesting that dissolved Fe is involved H_2 generation (Figure 3). Relatively high Fe concentrations (>0.1 mM), likely due to the effective dissolution of ferrous saponite under weakly acidic conditions, did not always result in rapid H_2 generation (Figure 3).
4. As for the mineral phases, only ferrous saponite among all the tested minerals demonstrated distinct H_2 generation triggered by the presence of H_2S (Figure 1). The lower initial abundances of ferrous saponite tend to result in lower H_2 concentrations (Figure 2). Sub-micrometer-sized pyrite is formed with the H_2 generation (Figure 4). Oxidation to Fe(III)-bearing materials also occurred around the pyrite particles (Figure 5).

Concerning points (1) and (2) above, one possible interpretation for the pH dependence on the reaction kinetics is that H_2 production may be controlled by the availability of HS^- rather than H_2S. HS^- is thermodynamically more stable at pH > 7 than H_2S while H_2S is more stable than HS^- at pH < 7. The point of zero charge (ZPC) of Na-smectite has been reported as 7.8–8.2 at an ionic strength of 0.001–0.1 (Arfaoui et al., 2012; Avena & De Pauli, 1998; Manohar et al., 2006). Assuming a similar ZPC value for ferrous saponite, the negative charge of its surface at high pH (>∼8) could inhibit the interaction of HS^- with ferrous saponite. Accordingly, H_2 generation could be optimal at circumneutral pH (∼7). This finding is contrasting to H_2 generation with troilite because the reaction of HS^- with troilite has been excluded by the large HOMO-LUMO gap (>+6 eV) (Rickard & Luther, 1997).

Concerning the point (3), one possible pathway that ferrous ion involved to form H_2 is the oxidization reaction as follows:

$$3Fe^{2+} + 4H_2O \rightarrow Fe_3O_4(\text{magnetite}) + 6H^+ + H_{2(g)}\,. \quad (4)$$

However, the fact that H_2 generation requires the presence of H_2S (point 1) suggests that Fe^{2+} would have contributed to H_2 production in a different pathway from the reaction (Equation 4). In addition, the generation of $6H^+$ suggests that the reaction (Equation 4) can proceed efficiently under high pH conditions (e.g., Seyfried

et al., 2007), while H_2 concentration increased more rapidly in the neutral pH condition in group II experiments than in the alkaline condition in group I experiments, despite the similar range of Fe concentration.

Concerning point (4), the fact that the initial amount of the mineral controlled the final H_2 concentration demonstrates that ferrous saponite is involved in the reaction. The low H_2 production in the experiments with magnetite also shows that ferrous saponite would play a role more than a source of dissolved Fe^{2+}. Given the formation of pyrite, the alternative reaction (Equation 4) to form H_2 is as follows:

$$Fe^{2+} + 2HS^- \rightarrow FeS_2 + H_{2(g)}, \tag{5}$$

in which both Fe^{2+} and HS^- react to form H_2 and pyrite. Given that ferrous saponite can be oxidized by the substitution of structural O^{2-} by OH^- (Sakuma et al., 2022), we propose that the following bulk H_2 generating reaction is consistent with our experimental observation in which the reaction (Equation 5) is involved:

$$\begin{aligned} &2Na_{0.5}\left(Mg_{1.5}\,Fe^{2+}_{1.5}\right)\left(Si_{3.5}Al_{0.5}\right)O_{10}(OH)_2 + Fe^{2+} + 2HS^- \\ &\rightarrow 2Na_{0.5}\left(Mg_{1.5}\,Fe^{2+}_{0.5}Fe^{3+}_{1.0}\right)\left(Si_{3.5}Al_{0.5}\right)O_{11}(OH) + FeS_2 + 2H_{2(g)}. \end{aligned} \tag{6}$$

In this reaction, ferrous saponite acts as (i) an electron donor to reduce HS^- and (ii) a source of dissolved iron to form pyrite. The stoichiometry of the reaction (Equation 6) indicates that 10 μmol of Fe^{2+} is required for a headspace of 60 mL to contain 8×10^3 ppm of H_2. This Fe supply corresponds to ∼1 mM of Fe^{2+} dissolution into a 10 mL fluid. This level of Fe^{2+} dissolution approximately corresponds to the measured Mg concentration in the fluid. Given the synthesized ferrous saponite composition of Fe:Mg = 1:1, Fe^{2+} supply via dissolution of saponite is consistent with the measured H_2 production. Reaction (Equation 6) might be described by excluding the reaction (Equation 5) as follows:

$$\begin{aligned} &2Na_{0.5}\left(Mg_{1.5}\,Fe^{2+}_{1.5}\right)\left(Si_{3.5}Al_{0.5}\right)O_{10}(OH)_2 \\ &\rightarrow 2Na_{0.5}\left(Mg_{1.5}\,Fe^{2+}_{0.5}Fe^{3+}_{1.0}\right)\left(Si_{3.5}Al_{0.5}\right)O_{11}(OH) + H_{2(g)}. \end{aligned} \tag{7}$$

However, the absence of H_2 generation in the experiments with ferrous saponite and without H_2S indicate that the reaction (Equation 7) does not proceed independently from pyrite formation. Although there is another possibility that ferrous saponite catalyzes reaction (Equation 5), our STXM results show that the Fe(III)-bearing feature was less significant in the solid sample retrieved after the reaction without H_2S. This observation supports the hypothesis that reaction (Equation 5) may stimulate the reaction (Equation 7) in the experiments with H_2S. We cannot rule out the intermediate formation of FeS mackinawite instead of the direct formation of pyrite in reactions (Equations 5 and 6), which may have happened on timescales shorter than the time interval of our experiments. Further work will be needed to assess if Fe^{2+} and HS^- form such a reaction intermediate in a maturation process to form pyrite.

4.2. Potential H_2 Yield on Mars

Our experimental results suggest that pre-existing ferrous saponite within the crust of early Mars may have formed H_2 if subsurface fluids that contain H_2S have intruded and interacted in the later stage after the saponite formation. H_2S in the fluids is likely supplied as a degassing species (Gaillard et al., 2013; Gaillard & Scaillet, 2009). In this section, we estimate the potential impact of this H_2 production process on early Mars.

We first assumed that H_2 production would be in a proportional relationship to the reactive amount of ferrous saponite based on our experimental results on the comparison of H_2 production for different initial amounts of ferrous saponite (Section 3.1). Figure 6 shows that H_2 production per 1 g of mineral reaches $(0.5–2) \times 10^{-1}$ mmol in most of the runs with H_2S, generally independent of fluid pH after a long reaction time, while it reaches below 3×10^{-3} mmol when magnetite or no H_2S is contained.

Concerning the amount of ferrous saponite within the Martian crust, previous remote sensing studies have interpreted that ferrous saponite has been generated globally within the Martian crust by Noachian, the era in which the active hydrothermal circulation at the subsurface is expected (Ehlmann et al., 2011; Michalski et al., 2013). Here, we defined the Global Equivalent Layer of Clay minerals (*GEL-C*) as the hypothetical

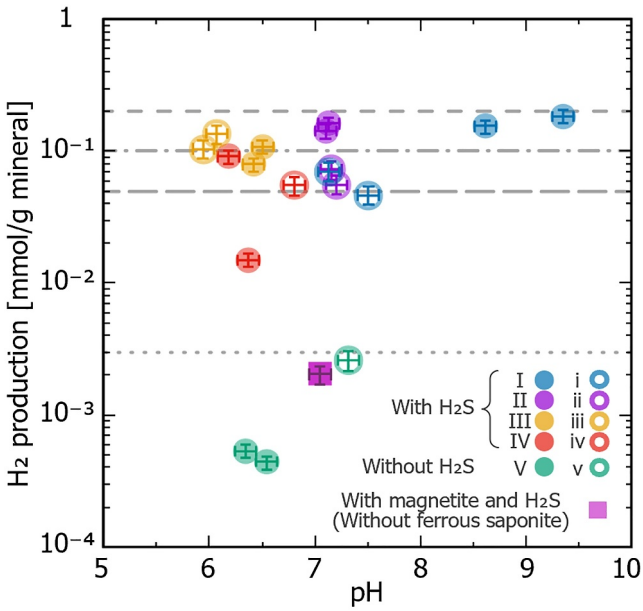

Figure 6. A summary of our results of H_2 production in the experiments with a reaction time longer than 1,300 hr, normalized with the mass of the mineral against the fluid pH. The measured H_2 concentrations are converted into the molar amounts using a headspace gas volume of 60 ± 1 mL. Each data point is from a single experiment with errors due to the uncertainties in quantitation and normalization. Gray broken/dotted lines represent H_2 production of 0.2, 0.1, 0.05, and 0.003 mmol g^{-1}.

thickness of clay minerals within the crust averaged throughout the planetary surface. Based on remote-sensing observations of canyons and craters on Mars, *GEL-C* can reach 5–10 km (Scheller et al., 2021). This range is consistent with the model results for clay mineral formation via interactions between a steam atmosphere and primitive crust (Cannon et al., 2017). The amount of reactive ferrous saponite in the mass M_{FeSap}, can be described as follows:

$$M_{\mathrm{FeSap}}(x) = \rho_{\mathrm{cr}} \times S_{\mathrm{Mars}} \times GEL\text{-}C \times x\,, \tag{8}$$

where ρ_{cr} is the density of the crust (assumed as 2.8 g cm^{-3}: Knapmeyer-Endrun et al., 2021) and S_{Mars} is the surface area of Mars (1.44×10^8 km^2). To deal with the uncertainty in the reaction completeness, the variable x was given as the mass fraction of ferrous saponite that interacted with H_2S-containing fluids relative to the total clay minerals represented as *GEL-C*. In addition to the uncertainty in the mineral composition of crustal clay minerals, they may have been buried 20–30 km below the surface (Cannon et al., 2017), while groundwater could have intruded shallower into the crust up to a depth of ∼10 km and not active well at a deeper layer due to the increased compaction (Kite & Melwani Daswani, 2019; Michalski et al., 2013), implying a certain portion of embedded clay would have not involved the interaction.

Given the H_2 production per mass of ferrous saponite, $R_{\mathrm{H_2:FeSap}}$, as a parameter, the global H_2 yield on Mars by the proposed reaction, $Y_{\mathrm{H_2}}$, can be calculated as follows:

$$Y_{\mathrm{H_2}}(x) = R_{\mathrm{H_2:FeSap}} \times M_{\mathrm{FeSap}}(x). \tag{9}$$

Figure 7 shows $Y_{\mathrm{H_2}}(x)$ calculated using *GEL-C* of 5 km and $R_{\mathrm{H_2:FeSap}}$ of 3×10^{-3} to 2×10^{-1} mmol g^{-1} (Figure 6). This figure compares with global H_2 yields from volcanic outgassing estimated by the previous studies (Grott et al., 2011; Scheller et al., 2021). With a nominal $R_{\mathrm{H_2:FeSap}}$ of 0.1 mmol g^{-1} (Figure 6), $Y_{\mathrm{H_2}}(x)$ could reach a comparable level with volcanic outgassing when x is larger than ∼10% (Figure 7). Although the value of x is difficult to constrain, this requirement (i.e., $x > 10\%$) might be unlikely because of the lack of evidence for global-scale hydrothermal alterations in the Martian crust. Our estimate suggests that the reaction with ferrous saponite may not have been an effective H_2 source to cause a strong greenhouse effect compared with volcanism. Rather, interactions between ferrous saponite and H_2S-containing fluids may be more significant as a source of locally concentrated H_2 on early Mars as they could provide chemical energy for chemoautotrophic life, such as methanogens.

There are many uncertainties in our estimate of H_2 production, particularly the assumption of $R_{\mathrm{H_2:FeSap}}$. For simplicity, no dependence on temperature, pressure, or other reaction conditions (e.g., water-to-rock ratios) was considered here. A supply of H_2S by fluids would be one of the most important factors that determines the H_2 production efficiency from saponites on early Mars. The outgassing rate of sulfur on early Mars has been estimated by extrapolation of the suggested sulfur outgassing rates of $\sim 10^9$ cm^{-2} s^{-1} on modern Earth (Halmer et al., 2002) and 10^{10}–10^{11} cm^{-2} s^{-1} on early Earth (Claire et al., 2014; Ranjan et al., 2018). An order of magnitude higher sulfur content of the Martian mantle than that of Earth, and an approximately 1:1 for a H_2S:SO_2 degassing ratio from Martian magma (oxygen fugacity of IW+1) could have resulted in H_2S supply flux of $\sim 10^{12}$ cm^{-2} s^{-1} (Gaillard & Scaillet, 2009, 2014). The provided H_2S can be effectively dissolved into alkaline fluids. Given low water-to-rock ratios in the subsurface and the presence of basalt, alkaline pH (7.5–10) should be achieved for subsurface (hydrothermal) fluids on Mars (Kikuchi & Shibuya, 2021; Kite & Melwani Daswani, 2019; Noda et al., 2022).

One possibility for increasing the total H_2 production is the dependence of $R_{\mathrm{H_2:FeSap}}$ on H_2S concentration in fluids. Since large fractions of unreacted ferrous saponite remained in our solid samples after the reactions

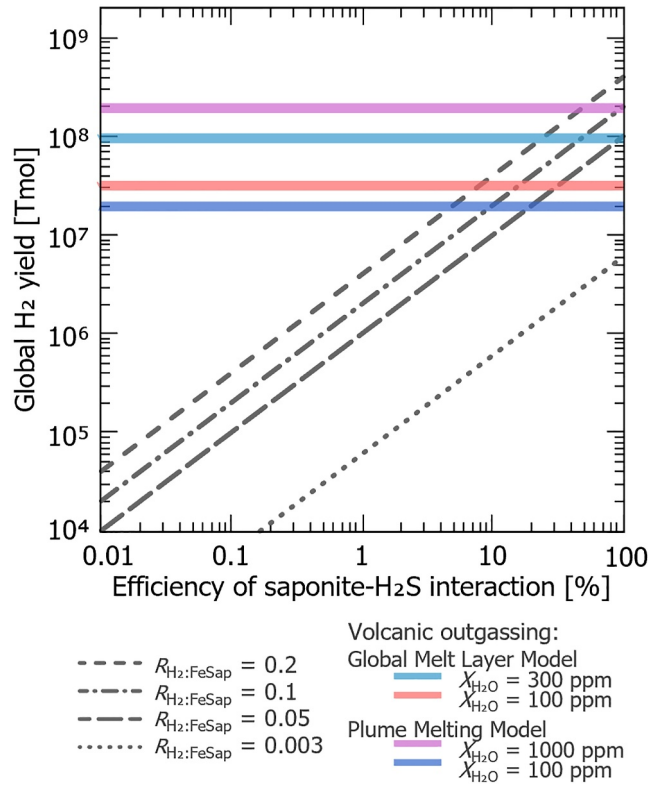

Figure 7. Estimated global H_2 yields occurs through the proposed reaction between ferrous saponite and H_2S-containing fluids (gray broken/dotted lines) and through volcanic outgassing during and after the Noachian period (after 4.1 Ga, colored solid lines). The former are calculated for $\boldsymbol{R_{H_2:FeSap}}$ values of 0.2, 0.1, 0.05, and 0.003 mmol g^{-1} as a function of the percentage of reacted ferrous saponite in crustal clay mineral (i.e., x in reaction Equations 8 and 9). The latter was obtained based on the parameterized model (Equation 18 and Table 3 in Grott et al., 2011) using H_2/H_2O ratio in volcanic gas for the oxygen fugacity of IW (iron–wüstite) + 1 (Gaillard & Scaillet, 2009; Hirschmann & Withers, 2008; Wordsworth et al., 2021) at typical outgassing conditions (1,450 K, 5 bar; Ramirez et al., 2014). The maximum and minimum estimates of initial mantle H_2O contents, $\boldsymbol{X_{H_2O}}$, for two cooling models were respectively applied, referring to a previous study (Scheller et al., 2021).

(Figure 5), $R_{H_2:FeSap}$ could become higher with a more effective supply of H_2S than those in our sealed experiments. The temperature dependence of $R_{H_2:FeSap}$ would be also crucial in evaluating the global effects of the H_2 formation process found in this study. $R_{H_2:FeSap}$ can vary largely in reality; however, the aim of our estimate is to provide a first-order approximation of H_2 production from ferrous saponite. A detailed evaluation of these assumptions requires further experimentation and is beyond the scope of this study.

5. Conclusions

This study investigated the reaction driven by redox-sensitive ferrous saponite to examine the role of ferrous saponite as an effective reductant in anoxic aqueous environments on early Mars. Based on a series of anaerobic hydrothermal experiments and molecular geochemical analysis, we discovered that ferrous saponite generates H_2 via interaction with H_2S-containing hydrothermal fluid at a relatively low temperature of 90°C. A comparison of the H_2 concentration in headspace gas, the concentration of Fe dissolved in the fluid, and the chemical species of iron in the recovered mineral among various reaction times, initial fluid and gas compositions, and contained amount of ferrous saponite were performed. These series of chemical and mineralogical analyses enabled us to propose that ferrous saponite is involved in the reaction by providing iron to form pyrite in addition to acting as an electron donor to generate H_2.

It is difficult to precisely quantify the impact of the H_2 production process we proposed on early Mars at this stage. The real reaction conditions on early Mars are not well constrained, while our experiments were conducted at only one pressure and temperature. Despite such uncertainties, the new pathway to convert H_2S into H_2 through fluid-

rock interaction under anoxic environments has a potential impact on planetary habitability. To evaluate whether the H_2 production via the proposed process can be important as a greenhouse effect gas, further experiments to investigate the H_2S and temperature dependence of this reaction would be crucial. Since ferrous saponite and volatile-containing fluids would have been available not only on early Mars but also on early Earth (Catalano, 2013; Gaillard & Scaillet, 2014), similar H_2 production could have occurred on these terrestrial planets.

Data Availability Statement

The analytical data generated for Figures 1–3 and 6 and the source data for Figures 4 and 5 are available for download from the open access repository (Noda et al., 2024).

Acknowledgments
This study was financially supported by KAKENHI JSPS (Grant JP19J22396, JP20H00195, JP21H04515, JP22K21344, JP22KJ1296, and JP23H00144). The STXM analyses were performed with the approval of the Photon Factory (No. 2018S001).

References

Andrews-Hanna, J. C., Phillips, R. J., & Zuber, M. T. (2007). Meridiani Planum and the global hydrology of Mars. *Nature*, *446*(7132), 163–166. https://doi.org/10.1038/nature05594

Arfaoui, S., Hamdi, N., Frini-Srasra, N., & Srasra, E. (2012). Determination of point of zero charge of PILCS with single and mixed oxide pillars prepared from Tunisian-Smectite. *Geochemistry International*, *50*(5), 447–454. https://doi.org/10.1134/S0016702912030020

Avena, M. J., & De Pauli, C. P. (1998). Proton Adsorption and Electrokinetics of an Argentinean Montmorillonite. *Journal of Colloid and Interface Science*, *202*(1), 195–204. https://doi.org/10.1006/jcis.1998.5402

Badaut, D., Besson, G., Decarreau, A., & Rautureau, R. (1985). Occurrence of a ferrous, trioctahedral smectite in recent sediments of Atlantis II deep, Red Sea. *Clay Minerals*, *20*(3), 389–404. https://doi.org/10.1180/CLAYMIN.1985.020.3.09

Barge, L. M., Flores, E., Baum, M. M., VanderVelde, D. G., & Russell, M. J. (2019). Redox and pH gradients drive amino acid synthesis in iron oxyhydroxide mineral systems. *Proceedings of the National Academy of Sciences of the United States of America*, *116*(11), 4828–4833. https://doi.org/10.1073/pnas.1812098116

Batalha, N., Domagal-Goldman, S. D., Ramirez, R., & Kasting, J. F. (2015). Testing the early Mars H_2-CO_2 greenhouse hypothesis with a 1-D photochemical model. *Icarus*, *258*, 337–349. https://doi.org/10.1016/j.icarus.2015.06.016

Bristow, T. F., Bish, D. L., Vaniman, D. T., Morris, R. V., Blake, D. F., Grotzinger, J. P., et al. (2015). The origin and implications of clay minerals from Yellowknife Bay, Gale crater, Mars. *American Mineralogist*, *100*(4), 824–836. https://doi.org/10.2138/am-2015-5077CCBYNCND

Cannon, K. M., Parman, S. W., & Mustard, J. F. (2017). Primordial clays on Mars formed beneath a steam or supercritical atmosphere. *Nature*, *552*(7683), 88–91. https://doi.org/10.1038/nature24657

Carter, J., Poulet, F., Bibring, J.-P., Mangold, N., & Murchie, S. (2013). Hydrous minerals on Mars as seen by the CRISM and OMEGA imaging spectrometers: Updated global view. *Journal of Geophysical Research: Planets*, *118*(4), 831–858. https://doi.org/10.1029/2012je004145

Catalano, J. G. (2013). Thermodynamic and mass balance constraints on iron-bearing phyllosilicate formation and alteration pathways on early Mars. *Journal of Geophysical Research: Planets*, *118*(10), 2124–2136. https://doi.org/10.1002/jgre.20161

Chaffin, M. S., Deighan, J., Schneider, N. M., & Stewart, A. I. F. (2017). Elevated atmospheric escape of atomic hydrogen from Mars induced by high-altitude water. *Nature Geoscience*, *10*(3), 174–178. https://doi.org/10.1038/ngeo2887

Chassefière, E., Langlais, B., Quesnel, Y., & Leblanc, F. (2013). The fate of early Mars' lost water: The role of serpentinization. *Journal of Geophysical Research: Planets*, *118*(5), 1123–1134. https://doi.org/10.1002/jgre.20089

Chassefière, E., Lasue, J., Langlais, B., & Quesnel, Y. (2016). Early Mars serpentinization-derived CH_4 reservoirs, H_2-induced warming and paleopressure evolution. *Meteoritics & Planetary Sciences*, *51*(11), 2234–2245. https://doi.org/10.1111/maps.12784

Chemtob, S. M., Nickerson, R. D., Morris, R. V., Agresti, D. G., & Catalano, J. G. (2015). Synthesis and structural characterization of ferrous trioctahedral smectites: Implications for clay mineral genesis and detectability on Mars. *Journal of Geophysical Research: Planets*, *120*(6), 1119–1140. https://doi.org/10.1002/2014JE004763

Chemtob, S. M., Nickerson, R. D., Morris, R. V., Agresti, D. G., & Catalano, J. G. (2017). Oxidative alteration of ferrous smectites and implications for the redox evolution of early Mars. *Journal of Geophysical Research: Planets*, *122*(12), 2469–2488. https://doi.org/10.1002/2017JE005331

Claire, M. W., Kasting, J. F., Domagal-Goldman, S. D., Stüeken, E. E., Buick, R., & Meadows, V. S. (2014). Modeling the signature of sulfur mass-independent fractionation produced in the Archean atmosphere. *Geochimica et Cosmochimica Acta*, *141*, 365–380. https://doi.org/10.1016/j.gca.2014.06.032

Cord-Ruwisch, R., Seitz, H.-J., & Conrad, R. (1988). The capacity of hydrogenotrophic anaerobic bacteria to compete for traces of hydrogen depends on the redox potential of the terminal electron acceptor. *Archives of Microbiology*, *149*(4), 350–357. https://doi.org/10.1007/bf00411655

Ehlmann, B. L., Mustard, J. F., Fassett, C. I., Schon, S. C., Head, J. W., III, Des Marais, D. J., et al. (2008). Clay minerals in delta deposits and organic preservation potential on Mars. *Nature Geoscience*, *1*(6), 355–358. https://doi.org/10.1038/ngeo207

Ehlmann, B. L., Mustard, J. F., Murchie, S. L., Bibring, J.-P. P., Meunier, A., Fraeman, A. A., & Langevin, Y. (2011). Subsurface water and clay mineral formation during the early history of Mars. *Nature*, *479*(7371), 53–60. https://doi.org/10.1038/nature10582

Ehlmann, B. L., Mustard, J. F., Swayze, G. A., Clark, R. N., Bishop, J. L., Poulet, F., et al. (2009). Identification of hydrated silicate minerals on Mars using MRO-CRISM: Geologic context near Nili Fossae and implications for aqueous alteration. *Journal of Geophysical Research*, *114*(E2). E00D08. https://doi.org/10.1029/2009JE003339

Fassett, C. I., & Head, J. W. (2008). The timing of martian valley network activity: Constraints from buffered crater counting. *Icarus*, *195*(1), 61–89. https://doi.org/10.1016/j.icarus.2007.12.009

Forget, F., Wordsworth, R., Millour, E., Madeleine, J.-B., Kerber, L., Leconte, J., et al. (2013). 3D modelling of the early Martian climate under a denser CO_2 atmosphere: Temperatures and CO_2 ice clouds. *Icarus*, *222*(1), 81–99. https://doi.org/10.1016/j.icarus.2012.10.019

Fuchs, G. (2011). Alternative pathways of carbon dioxide fixation: Insights into the early evolution of life? *Annual Review of Microbiology*, *65*(1), 631–658. https://doi.org/10.1146/annurev-micro-090110-102801

Fukushi, K., Sekine, Y., & Rampe, E. B. (2022). Reconstruction of pH, redox condition, and concentrations of major components in ancient liquid water from the Karasburg member, Murray formation, Gale Crater, Mars. *Geochimica et Cosmochimica Acta*, *325*, 129–151. https://doi.org/10.1016/j.gca.2022.02.005

Fukushi, K., Sekine, Y., Sakuma, H., Morida, K., & Wordsworth, R. (2019). Semiarid climate and hyposaline lake on early Mars inferred from reconstructed water chemistry at Gale. *Nature Communications*, *10*(1), 1–11. https://doi.org/10.1038/s41467-019-12871-6

Gaillard, F., Michalski, J., Berger, G., McLennan, S. M., & Scaillet, B. (2013). Geochemical reservoirs and timing of sulfur cycling on Mars. *Space Science Reviews*, *174*(1–4), 251–300. https://doi.org/10.1007/s11214-012-9947-4

Gaillard, F., & Scaillet, B. (2009). The sulfur content of volcanic gases on Mars. *Earth and Planetary Science Letters*, *279*(1), 34–43. https://doi.org/10.1016/j.epsl.2008.12.028

Gaillard, F., & Scaillet, B. (2014). A theoretical framework for volcanic degassing chemistry in a comparative planetology perspective and implications for planetary atmospheres. *Earth and Planetary Science Letters*, *403*, 307–316. https://doi.org/10.1016/j.epsl.2014.07.009

Grott, M., Morschhauser, A., Breuer, D., & Hauber, E. (2011). Volcanic outgassing of CO_2 and H_2O on Mars. *Earth and Planetary Science Letters*, *308*(3–4), 391–400. https://doi.org/10.1016/j.epsl.2011.06.014

Haberle, R. M. (1998). Early mars climate models. *Journal of Geophysical Research*, *103*(E12), 28467–28479. https://doi.org/10.1029/98je01396

Haberle, R. M., Zahnle, K., Barlow, N. G., & Steakley, K. E. (2019). Impact degassing of H_2 on early Mars and its effect on the climate system. *Geophysical Research Letters*, *46*(22), 13355–13362. https://doi.org/10.1029/2019GL084733

Halmer, M. M., Schmincke, H.-U., & Graf, H.-F. (2002). The annual volcanic gas input into the atmosphere, in particular into the stratosphere: A global data set for the past 100 years. *Journal of Volcanology and Geothermal Research*, *115*(3), 511–528. https://doi.org/10.1016/S0377-0273(01)00318-3

Hecht, M. H., Kounaves, S. P., Quinn, R. C., West, S. J., Young, S. M. M., Ming, D. W., et al. (2009). Detection of perchlorate and the soluble chemistry of Martian soil at the Phoenix lander site. *Science*, *325*(5936), 64–67. https://doi.org/10.1126/science.1172466

Heinen, W., & Lauwers, A. M. (1996). Organic sulfur compounds resulting from the interaction of iron sulfide, hydrogen sulfide and carbon dioxide in an anaerobic aqueous environment. *Origins of Life and Evolution of the Biosphere: The Journal of the International Society for the Study of the Origin of Life*, *26*(2), 131–150. https://doi.org/10.1007/BF01809852

Hirschmann, M. M., & Withers, A. C. (2008). Ventilation of CO_2 from a reduced mantle and consequences for the early Martian greenhouse. *Earth and Planetary Science Letters*, *270*(1), 147–155. https://doi.org/10.1016/j.epsl.2008.03.034

Hitchcock, A. P. (2009). aXis 2000 – Analysis of X-ray images and spectra. Retrieved from http://unicorn.mcmaster.ca/aXis2000.html

Hoehler, T. M., Alperin, M. J., Albert, D. B., & Martens, C. S. (2001). Apparent minimum free energy requirements for methanogenic Archaea and sulfate-reducing bacteria in an anoxic marine sediment. *FEMS Microbiology Ecology*, *38*(1), 33–41. https://doi.org/10.1111/j.1574-6941.2001.tb00879.x

Howard, A. D., Moore, J. M., & Irwin, R. P. (2005). An intense terminal epoch of widespread fluvial activity on early Mars: 1. Valley network incision and associated deposits. *Journal of Geophysical Research*, *110*(E12). E12S14. https://doi.org/10.1029/2005JE002459

Inskeep, W. P., Ackerman, G. G., Taylor, W. P., Kozubal, M., Korf, S., & Macur, R. E. (2005). On the energetics of chemolithotrophy in nonequilibrium systems: Case studies of geothermal springs in Yellowstone National Park. *Geobiology*, *3*(4), 297–317. https://doi.org/10.1111/j.1472-4669.2006.00059.x

Johnson, S. S., Mischna, M. A., Grove, T. L., & Zuber, M. T. (2008). Sulfur-induced greenhouse warming on early Mars. *Journal of Geophysical Research*, *113*(E8), 8005. https://doi.org/10.1029/2007je002962

Kasting, J. F. (1991). CO_2 condensation and the climate of early Mars. *Icarus*, *94*(1), 1–13. https://doi.org/10.1016/0019-1035(91)90137-i

Kikuchi, S., & Shibuya, T. (2021). Thermodynamic constraints on Smectite and Iron oxide formation at Gale Crater, Mars: Insights into potential free energy from Aerobic Fe oxidation in lake water–groundwater mixing zone. *Minerals*, *11*(4), 341. https://doi.org/10.3390/min11040341

Kitadai, N., Nakamura, R., Yamamoto, M., Okada, S., Takahagi, W., Nakano, Y., et al. (2021). Thioester synthesis through geoelectrochemical CO_2 fixation on Ni sulfides. *Communications Chemistry*, *4*(1), 1–9. https://doi.org/10.1038/s42004-021-00475-5

Kite, E. S., & Melwani Daswani, M. (2019). Geochemistry constrains global hydrology on Early Mars. *Earth and Planetary Science Letters*, *524*, 115718. https://doi.org/10.1016/j.epsl.2019.115718

Knapmeyer-Endrun, B., Panning, M. P., Bissig, F., Joshi, R., Khan, A., Kim, D., et al. (2021). Thickness and structure of the Martian crust from InSight seismic data. *Science*, *373*(6553), 438–443. https://doi.org/10.1126/science.abf8966

Kohyama, N., Shimoda, S., & Sudo, T. (1973). Iron-rich saponite (ferrous and ferric forms). *Clays and Clay Minerals*, *21*(4), 229–237. https://doi.org/10.1346/ccmn.1973.0210405

Koyama, S., Terada, N., Nakagawa, H., Kuroda, T., & Sekine, Y. (2021). Stability of atmospheric redox states of early mars inferred from time response of the regulation of H and O Losses. *The Astrophysical Journal*, *912*(2), 135. https://doi.org/10.3847/1538-4357/ABF0AC

Lanza, N. L., Wiens, R. C., Arvidson, R. E., Clark, B. C., Fischer, W. W., Gellert, R., et al. (2016). Oxidation of manganese in an ancient aquifer, Kimberley formation, Gale crater, Mars. *Geophysical Research Letters*, *43*(14), 7398–7407. https://doi.org/10.1002/2016GL069109

Manohar, D. M., Noeline, B. F., & Anirudhan, T. S. (2006). Adsorption performance of Al-pillared bentonite clay for the removal of cobalt(II) from aqueous phase. *Applied Clay Science*, *31*(3), 194–206. https://doi.org/10.1016/j.clay.2005.08.008

Mayhew, L. E., Ellison, E. T., McCollom, T. M., Trainor, T. P., & Templeton, A. S. (2013). Hydrogen generation from low-temperature water-rock reactions. *Nature Geoscience*, *6*(6), 478–484. https://doi.org/10.1038/ngeo1825

McCollom, T. M., & Shock, E. L. (1997). Geochemical constraints on chemolithoautotrophic metabolism by microorganisms in seafloor hydrothermal systems. *Geochimica et Cosmochimica Acta*, *61*(20), 4375–4391. https://doi.org/10.1016/S0016-7037(97)00241-X

Michalski, J. R., Cuadros, J., Bishop, J. L., Darby Dyar, M., Dekov, V., & Fiore, S. (2015). Constraints on the crystal-chemistry of Fe/Mg-rich smectitic clays on Mars and links to global alteration trends. *Earth and Planetary Science Letters*, *427*, 215–225. https://doi.org/10.1016/j.epsl.2015.06.020

Michalski, J. R., Cuadros, J., Niles, P. B., Parnell, J., Deanne Rogers, A., & Wright, S. P. (2013). Groundwater activity on Mars and implications for a deep biosphere. *Nature Geoscience*, *6*(2), 133–138. https://doi.org/10.1038/ngeo1706

Mustard, J. F., Murchie, S. L., Pelkey, S. M., Ehlmann, B. L., Milliken, R. E., Grant, J. A., et al. (2008). Hydrated silicate minerals on Mars observed by the Mars reconnaissance orbiter CRISM instrument. *Nature*, *454*(7202), 305–309. https://doi.org/10.1038/nature07097

Noda, N., Imamura, S., Sekine, Y., Kurisu, M., Fukushi, K., Terada, N., et al. (2019). Highly oxidizing aqueous environments on early Mars inferred from scavenging pattern of trace metals on manganese oxides. *Journal of Geophysical Research: Planets*, *124*(5), 1282–1295. https://doi.org/10.1029/2018je005892

Noda, N., Sekine, Y., Takahashi, Y., Fukushi, K., Sakuma, H., Kawai, T., et al. (2024). Hydrogen generation from ferrous saponite in reaction with H_2S-containing fluid: Relevance to early Martian habitability [Dataset]. https://doi.org/10.6084/m9.figshare.26011219

Noda, N., Sekine, Y., Tan, S., Kikuchi, S., Shibuya, T., Kurisu, M., et al. (2022). Characterization of groundwater chemistry beneath Gale Crater on early Mars by hydrothermal experiments. *Icarus*, *386*, 115149. https://doi.org/10.1016/j.icarus.2022.115149

Noda, N., Yamashita, S., Takahashi, Y., Matsumoto, M., Enokido, Y., Amano, K., et al. (2021). Anaerobic microscopic analysis of ferrous saponite and its sensitivity to oxidation by Earth's air: Lessons learned for analysis of returned samples from mars and carbonaceous asteroids. *Minerals*, *11*(11), 1244. https://doi.org/10.3390/min11111244

Ojha, L., Buffo, J., Karunatillake, S., & Siegler, M. (2020). Groundwater production from geothermal heating on early Mars and implication for early Martian habitability. *Science Advances*, *6*(49). eabb1669. https://doi.org/10.1126/sciadv.abb1669

O'Loughlin, E. J., Boyanov, M. I., Kemner, K. M., & Thalhammer, K. O. (2020). Reduction of Hg(II) by Fe(II)-Bearing Smectite Clay minerals. *Minerals*, *10*(12), 1079. https://doi.org/10.3390/min10121079

Poulet, F., Bibring, J.-P., Mustard, J. F., Gendrin, A., Mangold, N., Langevin, Y., et al. (2005). Phyllosilicates on Mars and implications for early Martian climate. *Nature*, *438*(7068), 623–627. https://doi.org/10.1038/nature04274

Quinn, R. C., Martucci, H. F. H., Miller, S. R., Bryson, C. E., Grunthaner, F. J., & Grunthaner, P. J. (2013). Perchlorate radiolysis on Mars and the origin of Martian soil reactivity. *Astrobiology*, *13*(6), 515–520. https://doi.org/10.1089/ast.2013.0999

Ramirez, R. M., Kopparapu, R., Zugger, M. E., Robinson, T. D., Freedman, R., & Kasting, J. F. (2014). Warming early Mars with CO_2 and H_2. *Nature Geoscience*, *7*(1), 59–63. https://doi.org/10.1038/ngeo2000

Rampe, E. B., Bristow, T. F., Morris, R. V., Morrison, S. M., Achilles, C. N., Ming, D. W., et al. (2020). Mineralogy of Vera Rubin ridge from the Mars science laboratory CheMin instrument. *Journal of Geophysical Research: Planets*, *125*(9). e2019JE006306. https://doi.org/10.1029/2019JE006306

Ranjan, S., Todd, Z. R., Sutherland, J. D., & Sasselov, D. D. (2018). Sulfidic anion concentrations on early earth for surficial origins-of-life chemistry. *Astrobiology*, *18*(8), 1023–1040. https://doi.org/10.1089/ast.2017.1770

Ravel, B., & Newville, M. (2005). ATHENA, artemis, hephaestus: Data analysis for X-ray absorption spectroscopy using IFEFFIT. *Journal of Synchrotron Radiation*, *12*(4), 537–541. https://doi.org/10.1107/S0909049505012719

Rickard, D. (1997). Kinetics of pyrite formation by the H_2S oxidation of iron (II) monosulfide in aqueous solutions between 25 and 125°C: The rate equation. *Geochimica et Cosmochimica Acta*, *61*(1), 115–134. https://doi.org/10.1016/s0016-7037(96)00321-3

Rickard, D., & Luther, G. W. (1997). Kinetics of pyrite formation by the H_2S oxidation of iron (II) monosulfide in aqueous solutions between 25 and 125°C: The mechanism. *Geochimica et Cosmochimica Acta*, *61*(1), 135–147. https://doi.org/10.1016/S0016-7037(96)00322-5

Righter, K., Yang, H., Costin, G., & Downs, R. T. (2008). Oxygen fugacity in the Martian mantle controlled by carbon: New constraints from the nakhlite MIL 03346. *Meteoritics & Planetary Sciences*, *43*(10), 1709–1723. https://doi.org/10.1111/j.1945-5100.2008.tb00638.x

Rivera Banuchi, V. B., Liu, W., Yee, N., Legett, C., Glotch, T. D., & Chemtob, S. M. (2022). Ultraviolet photooxidation of smectite-bound Fe(II) and implications for the origin of Martian nontronites. *Journal of Geophysical Research: Planets*, *127*(5). https://doi.org/10.1029/2021je007150

Sakuma, H., Morida, K., Takahashi, Y., Fukushi, K., Noda, N., Sekine, Y., & Tamura, K. (2022). Synthesis of ferrian and ferro-saponites: Implications for the structure of (Fe,Mg)-smectites formed under reduced conditions. *American Mineralogist*, *107*(10), 1926–1935. https://doi.org/10.2138/am-2022-8231

Salese, F., Pondrelli, M., Neeseman, A., Schmidt, G., & Ori, G. G. (2019). Geological evidence of planet-wide groundwater system on Mars. *Journal of Geophysical Research: Planets*, *124*(2), 374–395. https://doi.org/10.1029/2018JE005802

Scheller, E. L., Ehlmann, B. L., Hu, R., Adams, D. J., & Yung, Y. L. (2021). Long-term drying of Mars by sequestration of ocean-scale volumes of water in the crust. *Science*, *372*(6537), 56–62. https://doi.org/10.1126/SCIENCE.ABC7717

Seyfried, W. E., Foustoukos, D. I., & Fu, Q. (2007). Redox evolution and mass transfer during serpentinization: An experimental and theoretical study at 200°C, 500bar with implications for ultramafic-hosted hydrothermal systems at Mid-Ocean Ridges. *Geochimica et Cosmochimica Acta*, *71*(15), 3872–3886. https://doi.org/10.1016/j.gca.2007.05.015

Tarnas, J. D., Mustard, J. F., Sherwood Lollar, B., Bramble, M. S., Cannon, K. M., Palumbo, A. M., & Plesa, A.-C. (2018). Radiolytic H_2 production on Noachian Mars: Implications for habitability and atmospheric warming. *Earth and Planetary Science Letters*, *502*, 133–145. https://doi.org/10.1016/j.epsl.2018.09.001

Tosca, N. J., Ahmed, I. A. M. M., Tutolo, B. M., Ashpitel, A., & Hurowitz, J. A. (2018). Magnetite authigenesis and the warming of early Mars. *Nature Geoscience*, *11*(9), 635–639. https://doi.org/10.1038/s41561-018-0203-8

Treiman, A. H., Morris, R. V., Agresti, D. G., Graff, T. G., Achilles, C. N., Rampe, E. B., et al. (2014). Ferrian saponite from the Santa Monica Mountains (California, U.S.A., Earth): Characterization as an analog for clay minerals on Mars with application to Yellowknife Bay in Gale Crater. *American Mineralogist*, *99*(11–12), 2234–2250. https://doi.org/10.2138/am-2014-4763

Turbet, M., Boulet, C., & Karman, T. (2020). Measurements and semi-empirical calculations of $CO_2 + CH_4$ and $CO_2 + H_2$ collision-induced absorption across a wide range of wavelengths and temperatures. Application for the prediction of early Mars surface temperature. *Icarus*, *346*, 113762. https://doi.org/10.1016/j.icarus.2020.113762

Turbet, M., Forget, F., Head, J. W., & Wordsworth, R. (2017). 3D modelling of the climatic impact of outflow channel formation events on early Mars. *Icarus*, *288*, 10–36. https://doi.org/10.1016/J.ICARUS.2017.01.024

Vaniman, D. T., Bish, D. L., Ming, D. W., Bristow, T. F., Morris, R. V., Blake, D. F., et al. (2014). Mineralogy of a mudstone at Yellowknife Bay, Gale crater, Mars. *Science*, *343*(6169). 1243480. https://doi.org/10.1126/science.1243480

Wächtershäuser, G. (1992). Groundworks for an evolutionary biochemistry: The iron-sulphur world. *Progress in Biophysics and Molecular Biology*, *58*(2), 85–201. https://doi.org/10.1016/0079-6107(92)90022-x

Wan, M., Schröder, C., & Peiffer, S. (2017). Fe(III):S(-II) concentration ratio controls the pathway and the kinetics of pyrite formation during sulfidation of ferric hydroxides. *Geochimica et Cosmochimica Acta*, *217*, 334–348. https://doi.org/10.1016/j.gca.2017.08.036

Wordsworth, R., Forget, F., Millour, E., Head, J. W., Madeleine, J.-B., & Charnay, B. (2013). Global modelling of the early Martian climate under a denser CO_2 atmosphere: Water cycle and ice evolution. *Icarus*, *222*(1), 1–19. https://doi.org/10.1016/J.ICARUS.2012.09.036

Wordsworth, R., Kalugina, Y., Lokshtanov, S., Vigasin, A., Ehlmann, B., Head, J., et al. (2017). Transient reducing greenhouse warming on early Mars. *Geophysical Research Letters*, *44*(2), 665–671. https://doi.org/10.1002/2016GL071766

Wordsworth, R., Knoll, A. H., Hurowitz, J., Baum, M., Ehlmann, B. L., Head, J. W., & Steakley, K. (2021). A coupled model of episodic warming, oxidation and geochemical transitions on early Mars. *Nature Geoscience*, *14*(3), 127–132. https://doi.org/10.1038/s41561-021-00701-8

Zinder, S. H. (1993). Physiological ecology of methanogens. In *Methanogenesis* (pp. 128–206). Springer US. https://doi.org/10.1007/978-1-4615-2391-8_4

Zolotov, M. Y., & Mironenko, M. V. (2007). Timing of acid weathering on Mars: A kinetic-thermodynamic assessment. *Journal of Geophysical Research*, *112*(E7). https://doi.org/10.1029/2006je002882